2022

Investigating the capacitive properties of all-inorganic lead halides perovskite solar cells using energy band diagrams

Zahraa Ismail
zahraa.ismail@bue.edu.eg

eman Farouk Sawires
Helwan University, eman_sedhom@h-eng.helwan.edu.eg

Fathy Zaki Amer
Helwan University, Fathy_amer@h-eng.helwan.edu.eg

Sameh Osama Abdellatif Dr
The British University in Egypt

Investigating the capacitive properties of all-inorganic lead halides perovskite solar cells using energy band diagrams

Zahraa S. Ismail
Electrical Engineering Department
Faculty of Engineering and FabLab in the Center for Emerging Learning Technology (CELT)
The British University in Egypt
Cairo, Egypt
Zahraa.ismail@bue.edu.eg

Eman Sawires
Electronics and Communications Engineering Department
Faculty of Engineering, Helwan University
Cairo,Egypt
eman_sedhom@h-eng.helwan.edu.eg

Fathy Z. Amer
Electronics and Communications Engineering Department
Faculty of Engineering, Helwan University
Cairo,Egypt
Fathy_amer@h-eng.helwan.edu.eg

Sameh O. Abdellatif
Electrical Engineering Department
Faculty of Engineering and FabLab in the center for Emerging Learning Technology(CELT), The British University in Egypt(BUE)
Cairo,Egypt
Sameh.osama@bue.edu.eg

2022 IEEE International Conference on Semiconductor Electronics (ICSE) | 978-1-6654-8246-2/22/$31.00 ©2022 IEEE | DOI: 10.1109/ICSE56004.2022.9863109

***Abstract*— Capacitance response of perovskite solar cells (PSCs) can be oppressed to deduce underlying physical mechanisms, both in the materials at external interfaces and in bulk materials. Accordingly, this paper investigates the Capacitance-Voltage (C-V) characteristic curves of cesium lead halides ($CsPbX_3$: X = I, Br, or Cl) used as an active layer in PSCs. The SCAPS-1D simulator was used to harness the actual device ($CsPbX_3$: X = I Br, or Cl) with material parameters from previous experimental work. The energy-band diagrams, J-V curves, and C-V curves of the three PSC structures were constructed and compared to carry out and investigate their profound analyses.**

Keywords—Perovskite Solar cell, $CsPbX_3$, SCAPS-1D, Power Conversion Efficiency, Energy-band diagram, C-V characteristics.

I. INTRODUCTION

Hybrid organic-inorganic perovskite solar cells (PSCs) have drawn excessive attention in photovoltaic research as novel third-generation solar cells [1-8]. This is attributed to their tunable bandgap (E_g), significant absorption coefficient, low cost, small exciton binding energy, long carrier diffusion length, and more straightforward fabrication process than conventional crystalline silicon solar cells [8]. The recently reported PSCs' power conversion efficiency (PCE) has improved from 3.8% to 25.2% [9]. The volatile organic components induced (photo) chemical and thermal instability in hybrid organic-inorganic perovskite can be a predictable problem for its further commercialization [8]. Moreover, their deterioration at elevated temperatures and under-light soaking is still a series matter in commercial applications [10-12]. The thermal stability occurs from organic cations in perovskites, such as FA^+ and MA^+ cations, which may decay quickly at high temperatures [10]. Therefore, it is advisable to discover alternative materials or stabilize perovskite materials to reach the device's optimal performance (both stability and efficiency) [8, 12]. As a result, PSCs based on all-inorganic perovskite materials have drawn incredible attention due to their remarkable stability against thermal stress [6, 8, 11-13].

Lately, inorganic halide perovskite has been attained by substituting the volatile organic components with cesium (Cs) due to their superior photovoltaic performance, intrinsic inorganic stability with no chemical degradation, and no distortion of crystal lattice [8, 14-16]. The inorganic halide perovskites $CsPbX_3$ (X = I, Br, Cl) have been reported as early as 1893 to exhibit higher thermal stability than the hybrid organic-inorganic perovskites [6]. Their photoconductive properties and crystal structure were recognized in [8, 16].

Inorganic perovskites, $CsPbI_3$ with the cubic phase exhibits the most appropriate bandgap of 1.73 eV for photovoltaic applications [17]. The PCE for $CsPbI_3$-based PSC has improved from 2.9% to 19.03% since its first report in 2015 until writing this manuscript [8, 17]. $CsPbI_3$ demonstrates its great potential for high-efficiency inorganic PSCs with maximum current density per area of 22 mA/cm^2 and absorption edge at 720 nm [18]. However, it still has scarce stability under moist conditions; therefore, vital contributions are still required for achieving long-term stability [18].

Particularly, $CsPbBr_3$, with a high bandgap of approximately 2.3 eV, holds excellent moisture stability with a maximum current density per area of 9 mA/cm^2 and absorption edge at 520 nm [19]. It has been used to fabricate PSCs with high PCEs of 10.5% [19]. Alternatively, $CsPbCl_3$ exhibits the lowest efficiency with the greatest bandgap (E_g = 3 eV), with a maximum current density of 4 mA/cm^2 and an absorption edge at 300 nm [18].

Despite the remarkable efforts used to improve the stability issue of PSCs and to understand the deep analysis of the working of the cesium lead halides, the PSC structures with cesium lead halides are still insufficient for commercial applications. This work aims to deeply analyze the devices using capacitance-voltage (C-V), characteristics, and energy band diagrams. This analysis is based chiefly on conservative solid-state physics principles used for inorganic semiconductors., showing the PCE variations in the halide-based cells with deep interpretations.

978-1-6654-8246-2/22/$31.00 ©2022 IEEE

II. C-V SIMULATION MODELS

A. C-V Analytical Model

The capacitance-voltage profiling technique is a non-destructive, electric characteristic of the barrier capacitance of semiconductor junctions, such as semiconductor-metal in the form of p-n junction, or even metal-oxide-semiconductor (MOS) junctions [20]. It might impact the defect density and the flatting voltage where energy bands turned to be horizontal. It is restricted to a single frequency during the ac perturbation. Therefore, those reasons gave the technique a widespread, almost universal usage in the semiconductor industry. It can yield precise net active built-in potential (V_{bi}) and dopant distribution on planar structures [20].

The C-V characteristics are portioned into three main regions: the depletion region, charge-accumulation region, and charge-recombination region. The capacitance in the high-frequency portion is attributed to the permittivity in the perovskite active layer, an intrinsic property of the bulk material. Indeed, complete depletion arises at short circuit conditions and reverse (negative) applied voltage. In the depletion region, the capacitance acts to reach a graphical value, called geometrical capacitance, which only accounts for the sum of the dielectric contribution of each layer between the metallic electrodes [20]:

$$C_{ge} = \frac{A\,\varepsilon_r\varepsilon_0}{L} \quad (1)$$

ε_r is the relative dielectric constant of the medium, A is the effective area, L is the thickness of the medium, *and* ε_0 is the permittivity of the vacuum.

The photo-generated charge carriers tend to increment on the terminal electrode while varying the positive forward voltage up to its peak. This occurs because of the reduction in the built-in potential (V_{bi}). Consequently, an increase in the capacitance value is observed, with respect to the variation in the width of the depletion zone of a Schottky barrier. This refkects on the low-frequency range of the simulation in ordinary ionic conductors. This capacitance is independent of the active film thickness (L) and occurs at a short distance to the contact. A high V_{bi} is essential to obtain high PCE in PSCs with low mobility absorbers and prevent losses due to carrier recombination processes opposing charge extraction processes. V_{bi} and the density of fully ionized defect states (p- or n-doping level) N can be extracted from Mott-Schottky capacitance analysis due to Schottky contact formed at the perovskite/electrode interface [20]:

$$C^{-2} = \frac{2(V_{bi}-V)}{A^2\, e\, \varepsilon_r\varepsilon_0\, N} \quad (2)$$

.

Further increasing bias beyond this peak value, the photogeneratedphotogenerated charge carriers tend to recombine when V_{bi} is wholly diminished, which leads to a decrease in capacitance. Negative capacitances can be caused by recombination or self-heating.

B. SCAPS model

In this study, Solar Cell Capacitance Simulator (SCAPS-1D) was used to simulate the solar cell structure. SCAPS is a one-dimensional simulation program with seven semiconductor input layers [3, 21]. It was developed at the Department of Electronics and Information system, the University of Gent, Belgium [3, 21]. The solar cell used in the simulation is Au/NiO/absorber-layer/(mesoporous-compact-TiO_2)/FTO. The PSC structure is architectures are alternated such that the absorber layer was changed while the other parameters were kept the same. The three different absorber layers are $CsPbI_3$, $CsPbBr_3$, and $CsPbCl_3$, which are n-type material, p-type material, and p-type material, respectively, as proved in several works.

The solar cell illuminated through the transparent conductive oxide (TCO), which serves as a window layer, passes across the electron transport layer (ETL/TiO_2). The ETL is n-type with a total defect density N_t of $1x10^{15}$ cm^{-3} and enters the absorber layer to the hole transport layer (HTL/NiO), p-type with a total defect density N_t of $1x10^{15}$ cm^{-3}. The contact layer is gold (Au) with a work function of 5.1 eV.

The assumption for the simulation is under ambient temperature (300K) and at AM 1.5 G sun spectrum. The input parameters used for SCAPS simulation are carefully selected from the literature and previous experimental work [16, 22, 23]. The SCAPS simulator determined the absorption coefficients of the materials used based on the input. The energetic distribution of the absorber layers is Gaussian type, which has a characteristic energy value of 0.1 eV, and the capture cross-section for the holes and electrons is $1x10^{-19}$ cm^2 for all PSCs. The defect densities of $2.07x10^{12}$ cm^{-3},$1x10^{14}$ cm^{-3}, and $1x10^{15}$ cm^{-3} for $CsPbI_3$, $CsPbBr_3$, $CsPbCl_3$, respectively.

II. SIMULATION RESULTS AND DISCUSSIONS

A. C-V curve characteristic of the simulated device

A comparison of C-V characteristic curves can be beneficial to attain a better understanding of capacitance on the PSC, which is dependent on the applied voltage. The association was done by scanning a dc voltage (from -0.8 to 3 V) at a low alternating voltage of 50 mV at 1M Hz. As the bias increases from -0.8 V, the extension of the depletion region starts at the perovskite/electrode (Au) interface, then goes through the perovskite and finally TiO_2. Afterward, more charges will be accumulated by increasing the applied voltage, inducing higher capacitance until a specific voltage (V_{oc}) as 1.28V, 2.26V, 1.56V for $CsPbI_3$, $CsPbBr_3$, and $CsPbCl_3$, respectively.

The capacitance is extracted from figure 1 as $CsPbI_3$-based PSC has the least peak voltage, leading to the least accumulated capacitance on both interfaces compared to the other two PSC structures. However, $CsPbBr_3$ has the highest built-in voltage, which increases the peak voltage and maximum accumulation capacitance at the perovskite/TiO_2 interface compared to other PSCs. The calculated values of N and V_{bi} as ($1x10^{15}$ cm^{-3} and 1.28 V), ($1x10^{19}$ cm^{-3} and 2.26 V), and ($1x10^{15}$ cm^{-3} and 1.56 V) for $CsPbI_3$-, $CsPbBr_3$, $CsPbCl_3$-based PSCs and from solving equation 2. The results agree with the energetic offset between NiO/perovskite and perovskite/TiO_2 Fermi levels for $CsPbI_3$-based PSC and $CsPbCl_3$-based PSC and between perovskite/TiO_2 Fermi levels for $CsPbBr_3$-based PSC.

B. Energy band diagrams

The consideration of using two capacitors with different values was based on the predictable charge carrier.

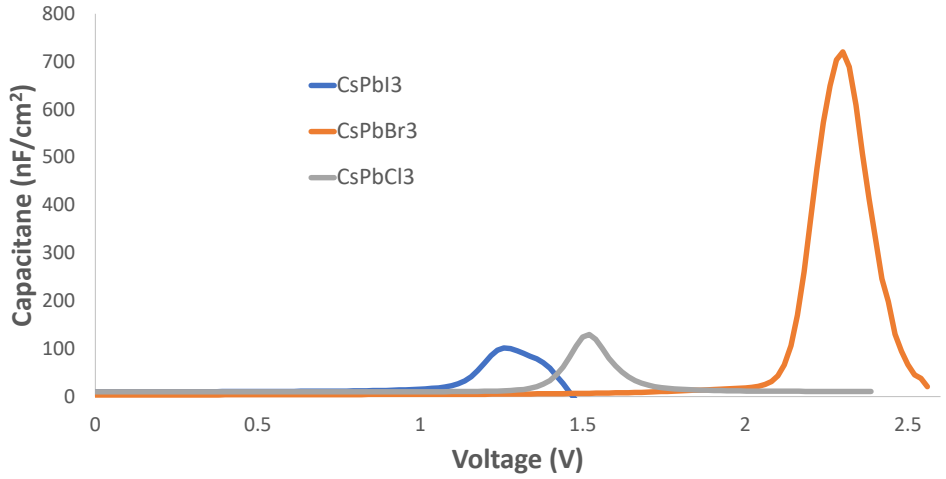

Fig. 1. C-V curve characteristics for three PSC structures with different Cesium Halides perovskite absorber layers.

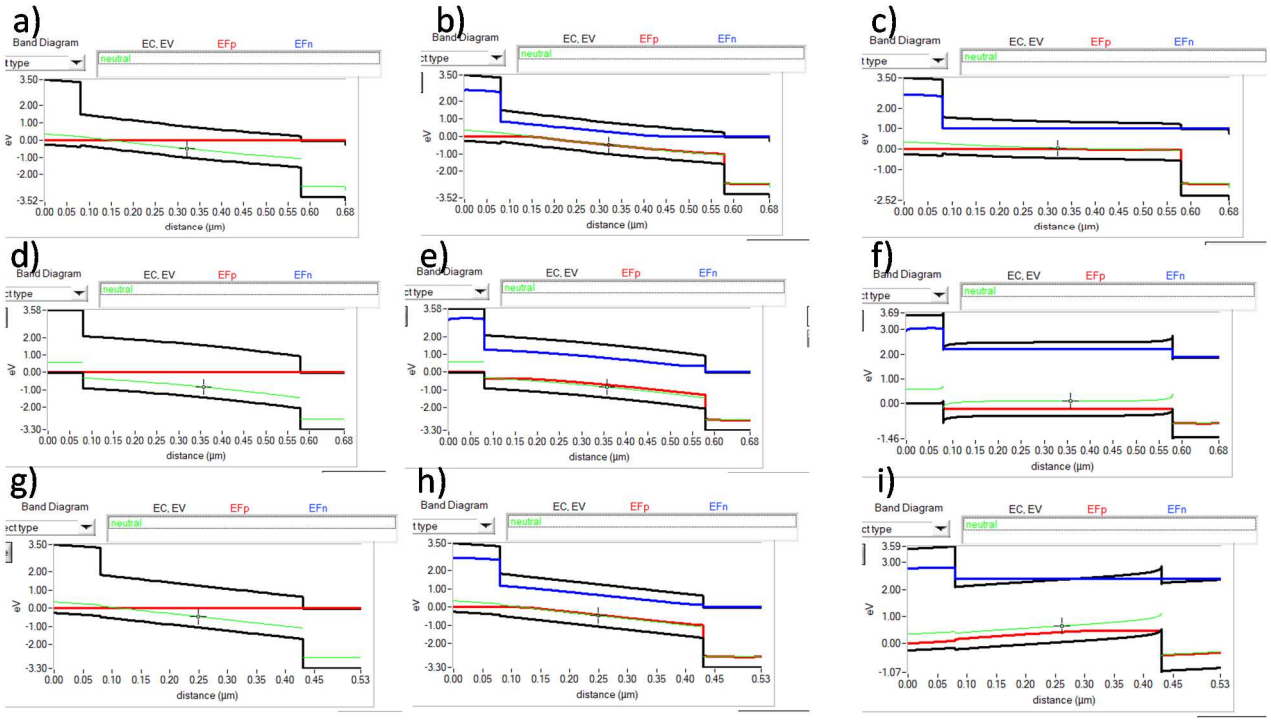

Fig. 2. Thermodynamic equilibrium at applied voltage of 0 V, (a) $CsPbI_3$, (d) $CsPbCl_3$, (g) $CsPbBr_3$. Applied voltage of 0 V under illumination (b) $CsPbI_3$, (e) $CsPbCl_3$, (h) $CsPbBr_3$. Applied voltage at V_{oc} under illumination (c) $CsPbI_3$, (f) $CsPbCl_3$, (i) $CsPbBr_3$.

Accumulation at the interface of NiO/perovskite and perovskite/ TiO_2. Figure 2 (a), (d), (g) shows energy band diagram for $CsPbI_3$-, $CsPbCl_3$-, $CsPbBr_3$-based PSCs at thermodynamic equilibrium under dark. Figure 2 (b), (e), (h) shows energy band diagram for $CsPbI_3$-, $CsPbCl_3$-, $CsPbBr_3$-based PSCs with zero applied voltage under illumination. Figure 2 (c), (f), (i) shows energy band diagram for $CsPbI_3$-, $CsPbCl_3$-, $CsPbBr_3$-based PSCs at applied voltage of V_{oc}. $CsPbI_3$-based PSC has the lowest voltage, leading to the least accumulated capacitance on both interfaces, as shown in fig. 2 (a). Therefore, it has the least band offset at NiO/perovskite and TiO_2/perovskite interfaces. It donates to low losses due to low series resistance, low surface recombination at the interface, and reduced grain boundary area. However, $CsPbBr_3$ has the highest built-in voltage, which decreases the peak voltage and maximum accumulation capacitance at the perovskite/TiO_2 interface due to the higher lattice disparity generated by different thermal expansion coefficients. This means that the noteworthy changes in the peak voltage are observed due to the change in the charge injection and non-aligned contact.

Moreover, the reduction of the electron affinity leads to an increase in the band offset, forming a spike as clearly shown in Figure 2 (i) at the perovskite/TiO_2 interface, acting as a barrier for photogeneratedphotogenerated electron flow toward the front electrode. This results in reducing both the electric field across the perovskite layer, built-in voltage, and high recombination of minority carriers. Therefore, the more accumulated charge led to lower PCE and FF. $CsPbCl_3$ shows

two capacitors at both interfaces, resulting in two spikes at both interfaces that act as a barrier for photogeneratedphotogenerated electron and hole flow toward the back electrode and front electrode, respectively.

III. Conclusion

This study explores the effect of the performance of $CsPbX_3$-based PSCs. Simulations were processed using SCAPS by, C-V curves and energy band diagrams of three PSC structures with $CsPbI_3$, $CsPbBr_3$, and $CsPbCl_3$. Perfect matching between our proposed model and experimental measurements from literature was observed. C-V curve characteristics and energy band diagrams were explored and discussed, showing that $CsPbI_3$-based PSC has the highest performance among other PSC structures.

Acknowledgment

The authors would like to acknowledge the support and contribution of the STDF in this work. As part of the STDF Project entitled, "Mesostructured Based Solar Cells for Smart Building Applications," Project ID#33502.

References

[1] Q. Lu, Z. Yang, X. Meng, Y. Yue, M. A. Ahmad, W. Zhang, *et al.*, "A review on encapsulation technology from organic light-emitting diodes to organic and perovskite solar cells," *Advanced Functional Materials,* vol. 31, p. 2100151, 2021.

[2] A. M. Mahran and S. O. Abdellatif, "Optoelectronic Modelling and Analysis of Transparency against Efficiency in Perovskites/Dye-based Solar Cells," in *2021 International Conference on Microelectronics (ICM)*, 2021, pp. 178-181.

[3] A. A. Eid, Z. S. Ismail, and S. O. Abdellatif, "Optimizing SCAPS model for perovskite solar cell equivalent circuit with utilizing Matlab-based parasitic resistance estimator algorithm," in *2020 2nd Novel Intelligent and Leading Emerging Sciences Conference (NILES)*, 2020, pp. 503-507.

[4] W. Zhu, W. Chai, D. Chen, J. Ma, D. Chen, H. Xi, *et al.*, "High-efficiency (> 14%) and air-stable carbon-based, all-inorganic CsPbI2Br perovskite solar cells through a top-seeded growth strategy," *ACS Energy Letters,* vol. 6, pp. 1500-1510, 2021.

[5] Z. Rao, W. Liang, H. Huang, J. Ge, W. Wang, and S. Pan, "High sensitivity and rapid response ultraviolet photodetector of a tetragonal CsPbCl 3 perovskite single crystal," *Optical Materials Express,* vol. 10, pp. 1374-1382, 2020.

[6] Y. An, C. Wang, G. Cao, and X. Li, "Heterojunction Perovskite Solar Cells: Opto-Electro-Thermal Physics, Modeling, and Experiment," *ACS Nano,* vol. 14, pp. 5017-5026, 2020.

[7] C. F. Wang, H. Li, M. G. Li, Y. Cui, X. Song, Q. W. Wang, *et al.*, "Centimeter-Sized Single Crystals of Two-Dimensional Hybrid Iodide Double Perovskite (4, 4-Difluoropiperidinium) 4AgBiI8 for High-Temperature Ferroelectricity and Efficient X-Ray Detection," *Advanced Functional Materials,* vol. 31, p. 2009457, 2021.

[8] P. Xu, "All-inorganic perovskite CsPbI2Br as a promising photovoltaic absorber: a first-principles study," *Journal of Chemical Sciences,* vol. 132, pp. 1-8, 2020.

[9] G.-H. Kim and D. S. Kim, "Development of perovskite solar cells with> 25% conversion efficiency," *Joule,* vol. 5, pp. 1033-1035, 2021.

[10] H. Wang, Z. Dong, H. Liu, W. Li, L. Zhu, and H. Chen, "Roles of organic molecules in inorganic CsPbX3 perovskite solar cells," *Advanced Energy Materials,* vol. 11, p. 2002940, 2021.

[11] J. Chen and W. C. Choy, "Efficient and Stable All-Inorganic Perovskite Solar Cells," *Solar RRL,* vol. 4, p. 2000408, 2020.

[12] T. Ma, S. Wang, Y. Zhang, K. Zhang, and L. Yi, "The development of all-inorganic CsPbX3 perovskite solar cells," *Journal of Materials Science,* vol. 55, pp. 464-479, 2020.

[13] Q. Chen, X. Yang, Y. Zhou, and B. Song, "Zwitterions: promising interfacial/doping materials for organic/perovskite solar cells," *New Journal of Chemistry,* vol. 45, pp. 15118-15130, 2021.

[14] D. Zhou, L. Tao, Z. Yu, J. Jiao, and W. Xu, "Efficient chromium ion passivated CsPbCl 3: Mn perovskite quantum dots for photon energy conversion in perovskite solar cells," *Journal of Materials Chemistry C,* vol. 8, pp. 12323-12329, 2020.

[15] A. Riquelme, L. J. Bennett, N. Courtier, M. Wolf, L. Contreras-Bernal, A. Walker, *et al.*, "Deducing the key physical properties of a perovskite solar cell from its impedance response: insights from drift-diffusion modelling," *arXiv: Applied Physics,* 2020.

[16] S. Ananthakumar, J. R. Kumar, and S. M. Babu, "Cesium lead halide (CsPbX3, X= Cl, Br, I) perovskite quantum dots-synthesis, properties, and applications: a review of their present status," *Journal of Photonics for Energy,* vol. 6, p. 042001, 2016.

[17] T. Zhang, M. I. Dar, G. Li, F. Xu, N. Guo, M. Grätzel, *et al.*, "Bication lead iodide 2D perovskite component to stabilize inorganic α-CsPbI3 perovskite phase for high-efficiency solar cells," *Science advances,* vol. 3, p. e1700841, 2017.

[18] D. Ren, H. Zhou, R. Chen, D. Wu, H. Pan, J. Zhang, *et al.*, "A-Site Substitute for Fabricating All-Inorganic Perovskite CsPbCl3 with Application in Self-Powered Ultraviolet Photodetectors," *The Journal of Physical Chemistry Letters,* vol. 13, pp. 267-273, 2022.

[19] Y. Zheng, X. Yang, R. Su, P. Wu, Q. Gong, and R. Zhu, "High-Performance CsPbIxBr3-x All-Inorganic Perovskite Solar Cells with Efficiency over 18% via Spontaneous Interfacial Manipulation," *Advanced Functional Materials,* vol. 30, p. 2000457, 2020.

[20] F. Recart and A. Cuevas, "Application of junction capacitance measurements to the characterization of solar cells," *IEEE transactions on electron devices,* vol. 53, pp. 442-448, 2006.

[21] M. Burgelman, K. Decock, A. Niemegeers, J. Verschraegen, and S. Degrave, "SCAPS manual," *February,* 2016.

[22] P. Yu, W. Zhang, F. Ren, J. Wang, H. Wang, R. Chen, *et al.*, "Strategies for highly efficient and stable cesium lead iodide perovskite photovoltaics: mechanisms and processes," *Journal of Materials Chemistry C,* vol. 10, pp. 4999-5023, 2022.

[23] Y. Zhang, C. Wu, D. Wang, Z. Zhang, X. Qi, N. Zhu, *et al.*, "High Efficiency (16.37%) of Cesium Bromide—Passivated All-Inorganic CsPbI2Br Perovskite Solar Cells," *Solar RRL,* vol. 3, p. 1900254, 2019.